Enhancing Fault Diagnosis of Rolling Element Bearings: A Novel SAE-DNN Approach with AdaBN for Domain Adaptation

Ali Davoodabadi[1] , Somaye Mohammadi[1], Hesam Addin Arghand[2], Mehdi Behzad[1*]

[1] Condition Monitoring Laboratory, Department of Mechanical Engineering, Sharif University of Technology, Tehran, Iran

[2] Assistant Professor, Department of Mechanical Engineering, Faculty of Engineering, University of Zanjan, Zanjan

* Correspondence: m_behzad@sharif.edu

Abstract:

Rolling element bearings (REBs) are critical components in rotating machinery, where reliable operation depends on accurate and timely fault diagnosis. This paper introduces a deep transfer learning framework designed to achieve robust cross-domain fault diagnosis across both laboratory and industrial environments. The framework integrates a Stacked Autoencoder (SAE) for hierarchical feature extraction with a Deep Neural Network (DNN) classifier, while leveraging Adaptive Batch Normalization (AdaBN) and selective fine-tuning of the output layer to effectively address domain shifts. The main contribution lies in the combined use of SAE-based feature learning, AdaBN-driven distribution alignment, and limited-sample fine-tuning using small sets of labeled industrial and fixed-condition laboratory data, enabling high diagnostic reliability under diverse operating conditions. To assess the contribution of each component, a baseline version of the model without the fine-tuning stage was also evaluated. The substantial performance degradation observed when testing on unseen target domains confirms the essential role of fine-tuning for achieving robust generalization. The proposed method was validated using laboratory datasets collected under variable and fixed operating conditions, as well as an industrial dataset consisting of four states, including healthy (H), inner race fault (IRF), outer race fault (ORF), and rolling element fault (REF). Experimental results show that the complete framework provides stable and accurate fault classification, achieving 92.65% accuracy on industrial data and 90.91% on fixed-condition laboratory data, consistently outperforming the baseline and conventional deep learning approaches in cross-domain scenarios.

Keywords: intelligent fault diagnosis; rolling element bearings; deep transfer learning; domain adaptation; stacked autoencoder; adaptive batch normalization

1. Introduction

Mechanical faults in industrial rotating machinery predominantly originate in shafts and REBs. Shaft defects, such as imbalance, misalignment, bending, cracks, eccentricity and torsional deformation, account for approximately 40 to 50 percent of mechanical failures, while REB faults contribute nearly 40 percent and typically affect the inner race, outer race, rolling elements or the cage. Each fault class produces characteristic vibration signatures that can serve as early indicators for condition monitoring and fault detection [1–4].

Recent advances in machine learning and deep learning have substantially improved the capability for automated fault diagnosis. Deep models, however, generally require large amounts of labeled data, and in industrial settings acquiring representative labeled failure data is often impractical or prohibitively expensive because it may require stopping equipment, creating faults intentionally or relying on time-consuming expert annotation. Consequently, transfer learning and domain adaptation have become essential tools for translating laboratory results into field-capable diagnostics by reducing distributional mismatch between source (laboratory) and target (industrial) data [5–23].

A broad range of transfer learning and deep-learning approaches has been applied to REB fault diagnosis. Shen et al. [24] proposed a method that combines singular value decomposition with Transfer AdaBoost. Zhang et al. [25] introduced the Wide Deep Convolutional Neural Network (WDCNN) employing wide kernels and adaptive batch normalization. Zhang et al. [26] developed an unsupervised domain adaptation approach based on subspace alignment. Zhang et al. [27] investigated parameter transfer from pretrained source models to novel operating conditions. Qian et al. [28] proposed a deep transfer network built from stacked autoencoders with adaptive batch normalization for adaptation without labeled target samples. Tong et al. [29] used fast Fourier transform, principal component analysis and maximum mean discrepancy (MMD) to extract transferable features. Li et al. [30] presented a domain-adaptive convolutional neural network. Yang et al. [31] combined MMD with pseudo-labeling to reduce feature distribution differences for unlabeled targets. Li et al. [32] proposed a nonnegativity-constrained sparse autoencoder for limited-label scenarios. Shao et al. [33] exploited time–frequency transforms together with pretrained networks. He et al. [34] developed an enhanced transfer autoencoder that includes SELU activations and non-negativity constraints. Zhao et al. [35] designed a multi-scale convolutional neural network with dilated convolutions and transferred it to target domains. Li et al. [36] proposed a cross-machine diagnosis framework that combines deep autoencoders and domain adaptation. Wu et al. [37] introduced the TMCD method using a batch-normalized LSTM together with adversarial strategies for distribution alignment. Dong and Li [38] addressed the small-sample problem by pretraining on simulated data and subsequently fine-tuning on a small quantity of real industrial data. Chen et al. [39] provided a comprehensive review of deep transfer learning for REB fault detection since 2016. Zhong et al. [40] proposed a domain-adversarial transfer learning model augmented with structural adjustment modules and automated architecture optimization via Optuna.

Beyond these works, recent studies have identified and developed a set of algorithmic components that are frequently effective in cross-domain REB diagnosis. Feisa et al. [41] synthesize this trajectory and classify methods into instance-, feature-, parameter- and adversarial-based families, noting the importance of multi-source adaptation, lightweight transferable architectures and adversarial strategies. Song et al. [42]

demonstrate that multi-scale attention combined with a joint adaptive adversarial loss, as in MAJATNet, can align both feature and label distributions and substantially improve unsupervised cross-domain performance. Che et al. [43] show that multi-layer, multi-kernel MMD integrated with adversarial domain classification achieves deeper alignment than single-layer MMD variants. Transforming one-dimensional vibration signals into two-dimensional time–frequency images or scattergrams and exploiting pretrained visual backbones has also emerged as a powerful approach: Deveci et al. [44] systematically compare time–frequency and scattergram transforms across CNN backbones and report marked gains in discriminability when imageized signals are used with transfer learning, and Xing et al. [45] synthesize RGB images from time, frequency and time–frequency channels and fine-tune ConvNeXt to improve feature representation without artificial augmentation.

Adversarial and GAN-style domain adaptation remain major strands of research. Guo et al. [46] review adversarial deep transfer learning and document both its ability to produce domain-invariant representations and the practical challenges it poses, notably training instability and difficulty of scaling to multiple target domains. Hybrid strategies that combine adversarial objectives with statistical discrepancy measures, for example joint MMD or JMMD, or conditional adversarial formulations, often yield improved stability and alignment, as demonstrated by Song et al. [42], Che et al. [43] and Tang et al. [47]. Attention modules, adaptive weighting and structured pseudo-labeling further enhance robustness to noisy, sparse or class-imbalanced target domains; Tang et al. [47] and Liu et al. [48] propose pipelines that combine continuous wavelet transform preprocessing, attention modules, conditional adversarial training, pseudo-labeling and locality-preserving projections to emphasize salient fault-relevant features in challenging target conditions.

Practical deployment considerations such as model footprint, training time and automated hyperparameter and architecture tuning have been addressed by multiple contributions. Li et al. [49] show that adaptive batch normalization, which replaces batch normalization statistics with domain-adaptive mean and variance, is an inexpensive and effective mechanism to reduce domain shift at inference time without costly retraining. Zhong et al. [50] combine domain-adversarial adaptation with automated structural adjustment and Optuna-driven search to reduce manual tuning and better accommodate complex target domains. Lightweight architectures such as MAJATNet together with adaptive batch normalization provide pragmatic pathways toward fieldable systems.

Despite these advances, a persistent limitation constrains generalizability. Many studies continue to validate methods primarily on standard laboratory benchmarks, most notably the Case Western Reserve University REB dataset [51]. This dataset lacks substantial variation in radial load and exhibits limited shaft speed variability. As a result, algorithms that perform well on such benchmarks frequently suffer significant accuracy degradation when transferred to heterogeneous, unlabeled industrial data. This shortcoming highlights the need for research that evaluates methods on more industrially representative datasets, conducts comprehensive assessments under varied operating regimes, and develops more robust transfer strategies.

To address these challenges, this study proposes an advanced transfer-learning framework integrating hierarchical feature extraction, domain adaptation, and selective fine-tuning of the classifier output layer using limited labeled samples from both industrial and laboratory datasets. A SAE is first used to extract robust hierarchical features, which are then fed into a deep neural network classifier. Adaptive Batch Normalization (AdaBN) is employed to align feature distributions between the source and target domains.

Fine-tuning only the output layer with a small number of labeled samples enables efficient adaptation to new domains without retraining the entire model. A key contribution of this work is the comprehensive validation performed on laboratory datasets under both variable and fixed operating conditions, in addition to real industrial data. Experimental results demonstrate that the proposed framework achieves high diagnostic accuracy across multiple fault types, including inner race faults, outer race faults, rolling element faults, and healthy conditions, while maintaining strong robustness under diverse operational scenarios.

The remainder of the paper is organized as follows. Section 2 presents the proposed methodology. Section 3 details the experimental setups and data collection procedures. Section 4 provides implementation details and validation results on laboratory datasets with variable and fixed operating conditions, as well as on industrial datasets. Section 5 concludes the study and discusses directions for future research.

2. Proposed Method

The proposed approach for fault detection in REBs comprises an integrated framework, consisting of three sequential stages:

- (Section 2.1) Feature Extraction with SAE: A SAE is employed in an unsupervised manner to extract hierarchical and robust features from vibration signals under variable laboratory conditions
- (Section 2.2) DNN Training and Domain Alignment with AdaBN: This stage involves initializing a DNN with the extracted features and training it with labeled laboratory data, while AdaBN is applied to align feature distributions between laboratory and industrial domains.
- (Section 2.3) Output Layer Fine-Tuning with Labeled Industrial Data: Only the output layer is fine-tuned using a limited set of labeled industrial samples to enhance classification accuracy, while the feature extraction layers remain frozen.

2.1. **Feature Extraction with SAE**

In this study, a SAE is employed to extract hierarchical and nonlinear features from vibration signals of REBs. SAE is chosen because, unlike linear methods such as PCA, it can learn complex latent representations of the data and provide well-initialized weights for DNNs, thereby mitigating issues such as vanishing gradients and slow convergence. Initially, the raw vibration signals are transformed into the frequency domain using the FFT. Variations in rotational speed, however, introduce frequency shifts and amplitude distortions. To compensate for these effects, the spectra are first normalized with respect to their corresponding rotational speed and then resampled through linear interpolation to a reference speed of 25 Hz. This process ensures alignment across different speeds while preserving fault-related features. The preprocessed spectra are then fed into the SAE. The proposed SAE architecture consists of three stacked autoencoders. The FFT spectrum, with a length of 4081, serves as the input, and the hidden layers contain 512, 256, and 128 neurons, respectively. Each autoencoder comprises an encoder and a decoder. Encoder maps the input vector x_i to a compact latent representation h_i as formulated as follows:

$$h_i = f(W_e * x_i + b_e)_i \tag{1}$$

where f is the ReLU activation function, and W_e and b_e denote the encoder weights and Biases. The decoder attempts to reconstruct the original input as formulated in Equation (2):

$$\acute{x}_i = g(W_d * x_i + h_d)_i \quad (2)$$

Where g is also the ReLU activation function, and W_d and h_d represent the decoder Weights and Biases. The training objective minimizes the reconstruction error as formulated as:

$$L_{AE} = \sum_{i=1}^{N} \frac{1}{N} \|x_i - \acute{x}_i\|^2 \quad (3)$$

To enhance training stability and accelerate convergence, Batch Normalization (BN) is applied in the encoder layers. For a mini-batch of size mmm, the batch mean is computed as formulated in Equation (4):

$$\mu_B = \sum_{i=1}^{m} \frac{1}{m} h_i \quad (4)$$

The batch variance is then calculated as given in the following relation:

$$\sigma_B{}^2 = \sum_{i=1}^{m} \frac{1}{m} (h_{i-}\mu_B)^2 \quad (5)$$

The input is normalized using the batch statistics as described as:

$$\acute{h}_i = \frac{h_i - \mu_B}{\sqrt{\sigma_B{}^2 + \epsilon}} \quad (6)$$

Finally, learnable parameters γ and β are applied to scale and shift the normalized outputs, as formulated as:

$$y_i = \acute{h}_i \gamma + \beta \quad (7)$$

These BN parameters (γ , β) are updated together with the encoder weights during training. This mechanism stabilizes the internal feature distributions and enables more effective learning. The SAE is trained using a greedy layer-wise pretraining strategy, where each autoencoder is trained independently, and only the encoder is retained. The output of each trained encoder serves as the input to the next, forming a hierarchical feature extractor. After pretraining, the three encoders are stacked to form the full SAE, and the decoders are discarded. The resulting encoders provide compact, discriminative feature representations and serve as initialization for the subsequent DNN. As illustrated in Figure 1, the SAE compresses the input dimensionality through four layers of sizes *N1*=4081, *N2*=512, *N3*=256, and *N4*=128. All encoder weights W and BN parameters γ, β are updated during training, enabling the SAE to learn informative features that capture latent patterns and improve downstream fault-classification performance.

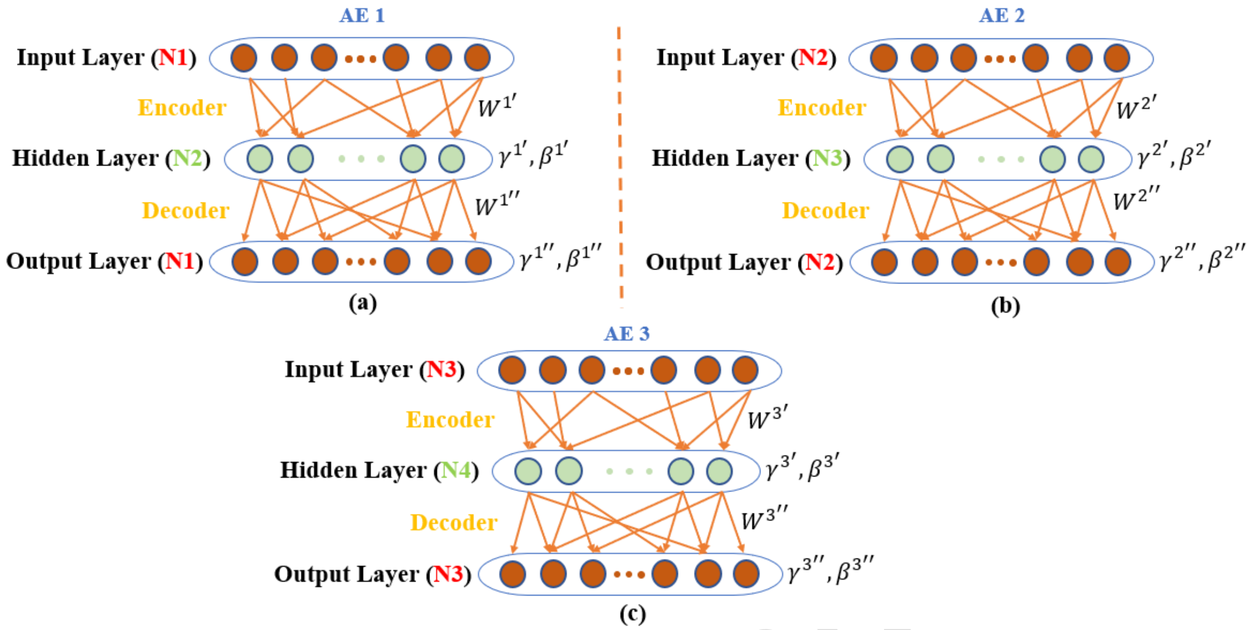

Figure 1. Architecture of the SAE for Feature Extraction and Initialization of the DNN

2.2. DNN Training on the Source Domain

After extracting hierarchical features using the SAE, the trained encoder weights and biases are transferred to a DNN and used as initialization for supervised training. This initialization enhances convergence speed and improves optimization stability. The DNN architecture consists of the stacked SAE encoder layers followed by a fully connected output layer with a Softmax classifier. During training on source-domain data (laboratory data under variable operating conditions), the weights and biases of all layers are updated via backpropagation using the Cross-Entropy loss function. In layers containing Batch Normalization (BN), the mean and variance are computed independently for each mini-batch, and the learnable BN parameters (γ and β) are updated jointly with the network weights. This ensures stable feature distributions during training and improves discriminative capability. By initializing the DNN with pretrained SAE parameters and jointly optimizing all weights, biases, and BN parameters, the network effectively learns robust hierarchical representations of vibration signals. As a result, the model achieves high fault-classification accuracy across a wide range of source-domain operating conditions.

2.3. Domain Adaptation and Fine-Tuning with Target Data

To transfer the trained model from the source domain to the target domain, a small set of labeled target samples is used to fine-tune only the output layer. In this study two target datasets are considered, industrial data and laboratory data collected under fixed operating conditionsPrior to fine-tuning, AdaBN is applied to align the internal feature distributions of the pretrained network with those of the target domain. Unlike standard Batch Normalization, where the mean and variance are computed from source-domain training data, AdaBN replaces these statistics with those computed from the target-domain samples. This substitution aligns the normalization process with the statistical properties of the target domain without modifying any of the pretrained network parameters. During AdaBN alignment, all encoder weights, classifier weights, and BN learnable parameters (γ and β) remain frozen; only the BN normalization statistics are replaced. For both target datasets, the mean and variance are computed exclusively from the small subset of samples used for fine-tuning, ensuring that no information from the final test sets is introduced.

After AdaBN alignment, only the weights and biases of the output layer are updated through backpropagation using the limited labeled target samples. The feature-extraction layers remain frozen to preserve the discriminative hierarchical representations learned from the source domain. During the final testing phase, the BN mean and variance are again replaced with those computed from the same fine-tuning subset. Importantly, unlabeled industrial test samples and fixed-condition laboratory test samples are never used for updating BN statistics or network parameters. All weights, including those of the output layer, remain fixed during testing; only input normalization follows the AdaBN-adjusted statistics. This ensures that the model is evaluated strictly on unseen data while benefiting from domain-consistent normalization. As illustrated in Figure 2, the proposed framework operates through three main stages. First, vibration signals are transformed into the frequency domain and used to pretrain a SAE via greedy layer-wise training. Second, the pretrained encoders are integrated into a DNN and trained with labeled source-domain data under variable conditions. Finally, AdaBN and selective fine-tuning adapt the classifier to each target domain (industrial and fixed-condition laboratory data), enabling robust performance under real-world and distribution-shifted environments.

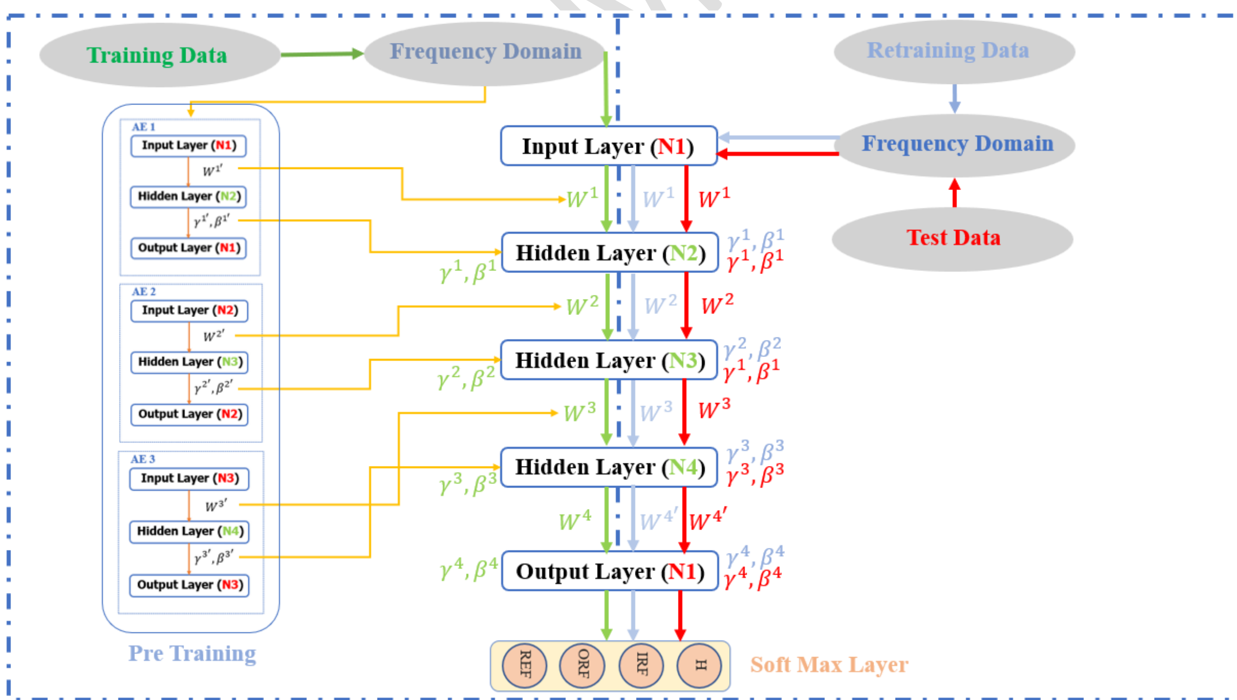

Figure 2. Overall framework of the proposed fault diagnosis algorithm, showing SAE pretraining, DNN training, and fine-tuning of the output layer with domain adaptation via AdaBN

As detailed in Table 1, the proposed fault diagnosis framework consists of a hierarchical stack of three SAE encoder layers, followed by a fully connected DNN output layer. The table provides comprehensive layer-wise specifications, including the number of neurons, output dimensionalities, trainable weights, biases, and BN parameters. In particular, the "Weights + Bias" column denotes the total number of trainable parameters associated with the weights and biases of each layer, the "BN Params" column indicates the number of trainable BN parameters (γ and β), and the "Total Params" column represents the cumulative count of all parameters within the layer. The table further indicates the trainable status of each layer across three distinct training phases: SAE pretraining, source domain DNN training, and fine-tuning with labeled target data, including both industrial and fixed-condition laboratory samples. During SAE pretraining, all weights and BN parameters are updated to hierarchically capture informative feature representations at multiple abstraction levels. In the source domain training phase, the weights and biases of all SAE encoder layers, together with the DNN output layer, are jointly optimized to align learned representations for accurate fault classification. In the fine-tuning stage, only the DNN output layer is updated with labeled target domain data, while all feature extraction layers and BN parameters remain frozen. This selective updating preserves the robust and discriminative features learned from the source domain, enabling effective cross-domain knowledge transfer while mitigating catastrophic forgetting.

Table 1. Architecture and training stages of the proposed fault diagnosis model

Stage	**Layer**	**Neurons/Filters**	**Output Shape**	**Weights + Bias**	**BN Params**	**Total Params**	Description
SAE Pretraining	1	512	(4081, 512)	2,088,384	1,024	2,089,408	First-level feature extraction; weights and BN parameters (γ/β) updated during pretraining
	2	256	(512, 256)	131,328	512	131,840	Second-level feature extraction; weights and BN parameters updated
	3	128	(256, 128)	32,896	256	33,152	Third-level feature extraction; weights and BN parameters updated
Source Domain Training	1	512	(4081, 512)	2,088,384	1,024	2,089,408	SAE layer 1 weights, biases, and BN updated along with DNN output layer
	2	256	(512, 256)	131,328	512	131,840	SAE layer 2 weights, biases, and BN updated
	3	128	(256, 128)	32,896	256	33,152	SAE layer 3 weights, biases, and BN updated
	4	4	(128, 4)	516	8	524	Fully connected DNN output layer; weights, biases, and BN updated for fault classification
Fine-tuning with Target Data	1	512	(4081, 512)	Frozen	Frozen	2,089,408	SAE encoder layers frozen; BN parameters γ/β fixed
	2	256	(512, 256)	Frozen	Frozen	131,840	SAE layer 2 frozen
	3	128	(256, 128)	Frozen	Frozen	33,152	SAE layer 3 frozen

	4	4	(128, 4)	516	8	524	Only DNN output layer updated with labeled target (industrial) data

Table 2 summarizes the critical hyperparameters and training configurations used across all stages, including the number of epochs, batch size, optimizer, loss function, validation split, and early stopping criteria. Each hyperparameter plays a key role in ensuring stable and efficient training. The number of epochs controls the total number of passes over the dataset, with fewer epochs used during fine-tuning to prevent overfitting on the target domain. The batch size is set to 32, determining the number of samples processed per iteration and ensuring stable gradient estimates. The Adam optimizer is employed for adaptive gradient-based optimization of network parameters. Categorical cross-entropy is used as the loss function to handle multi-class fault classification tasks. A validation split of 10 percent monitors performance and guides early stopping, which is implemented with a patience of three epochs, terminating training if the validation loss does not improve, thereby preventing overfitting and enhancing generalization.

Table 2. Key Optimization Hyperparameters and Training Configurations

Parameter	Value	Description / Role
Number of Epochs	50 (SAE Pretraining), 50 (Source Domain Training), 30 (Fine-tuning)	Total passes over the dataset; reduced during fine-tuning to prevent overfitting on target domain
Batch Size	32	Number of samples processed per iteration; ensures stable gradient estimation
Optimizer	Adam	Adaptive gradient-based optimization of network weights and biases; learning rate adjustable
Loss Function	Categorical Cross-Entropy	Suitable for multi-class fault classification tasks
Validation Split	0.1	10% of training data reserved for validation to monitor model performance and guide early stopping
Early Stopping	Patience = 3	Training stops if validation loss does not improve for 3 consecutive epochs, preventing overfitting

3. Experimental Setup and Data Acquisition

This section presents the experimental setups and data acquisition procedures used to evaluate the performance of the proposed fault diagnosis models. Section 3.1 introduces the laboratory test rig and details the procedures followed during experiments. Section 3.2 describes the acquisition of laboratory data under variable operating conditions and its role in model training and evaluation. Section 3.3 outlines the collection and preprocessing of industrial data under diverse operational conditions to ensure its suitability for validating model performance in real-world scenarios. Section 3.4 introduces an additional set of laboratory data obtained under fixed operating conditions, which is employed to further examine the model's robustness and generalization capability across different operational domains.

3.1. Laboratory Test Setup

To evaluate the proposed model, a specialized REB test setup was developed at the Condition Monitoring Laboratory, capable of varying load and speed during the REB degradation process (Figure 3). Emergency load control is provided by a computer-managed hydraulic power pack system. The target REB is positioned between two supporting REBs, while rotational speed is precisely controlled via the motor drive.

This setup allows real-time measurement of speed as well as vertical and horizontal vibrations of the applied load. For this study, data were collected from a horizontal accelerometer sensor aligned with the applied load.

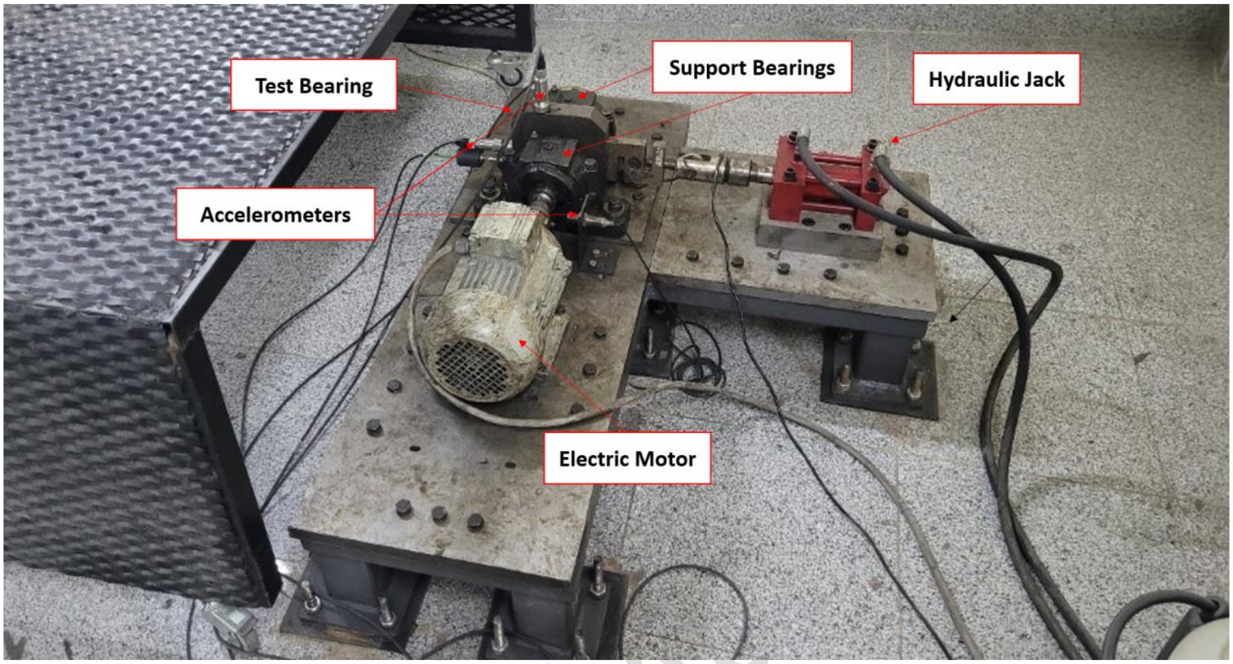

Figure 3. Schematic of the accelerated life testing setup for REBs on the experimental test rig.

Vibration of test REB is measured using the SDT Vigilant data acquisition system [52], while the HS1001005008 sensor was employed to capture the vibration signals. The signals were sampled at a frequency of 25,600 Hz to ensure high-resolution data collection. In this study, a self-aligning double-row REB was utilized for testing purposes. Figure 4 illustrates the artificial faults introduced on the REB components to simulate typical degradation patterns.

a)  b)  c) 

Figure 4. Artificially induced damages in the test rolling element bearing (REB), showing (a) Inner Race Fault (IRF), (b) Rolling Element Fault (REF), and (c) Outer Race Fault (ORF).

Table 3 presents the dimensions of the ETN9 REB, along with the characteristic frequencies corresponding to the IRF, ORF, and REF, as well as the dynamic specifications of the test REB, providing a comprehensive overview of its geometric and operational properties essential for accurate experimental analysis.

Table 3. Specifications of the ETN9 REB 1210 [53].

Category	Parameter	Symbol	Value (rpm)	Unit
Dimensional Specifications	Outer Diameter	O	90	mm
	Inner Diameter	I	50	mm
	Width	B	20	mm
	Number of Balls	N	34	–
Rotational Speed	Motor Speed	–	60	rpm
Frequency Specifications	Ball Pass Frequency – Outer	BPFO	435.6	rpm
	Ball Pass Frequency – Inner	BPFI	556.8	rpm
	Ball Spin Frequency	BSF	392.4	rpm
	Fundamental Train Frequency	FTF	25.2	rpm
Dynamic Specifications	Static Load Capacity	C_0	9.15	kN
	Dynamic Load Capacity	C	26.5	kN

3.2. Introduction to Data Acquisition Scenarios

From a practical perspective, the specific type of fault, meaning which component is affected, has limited significance because degradation in any of the inner race, outer race, or rolling element generally results in the same recommendation, which is to replace the REB. Nevertheless, accurately identifying the fault type allows experts and machine owners to make more informed and confident maintenance decisions. The rationale for incorporating variable operating conditions is to enable the developed model to perform intelligent fault detection under diverse conditions and thus reduce its dependence on specific operational environments. For this study, artificial faults were introduced into the REBs, and laboratory tests were performed under four distinct fault conditions, namely H, IRF, ORF, and REF, across 36 different operating scenarios as shown in Figure 5.

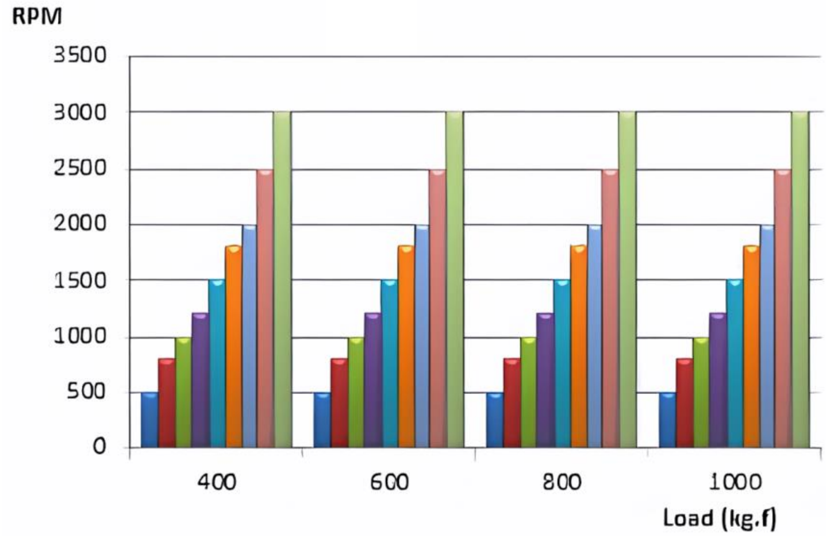

Figure 5. Number of data samples recorded for each of the four conditions (healthy, IRF, REF, and ORF) across nine rotational speeds and five different load levels.

In these experiments, rotational speed ranged from 500 rpm to 3000 rpm, while the applied load varied from 400 kgf to 1000 kgf. Unlike the CWRU dataset, where rotational speed is limited to a range of 1720 to 1797 rpm with variations below five percent and the radial load remains constant, this study investigates a broader spectrum of speeds and loads to more accurately examine their impact on fault detection. This expanded dataset allows for a more comprehensive evaluation of model performance under variable operating conditions. Measurements were simultaneously recorded using three vibration sensors aligned along three orthogonal directions, which are vertical, horizontal, and axial. A total of 4741 datasets were collected for all four fault conditions, encompassing all combinations of load and speed. Each time-domain recording lasted 160 milliseconds, with 4096 samples collected per measurement. Moreover, this dataset is planned to be publicly released in the future to support further research in fault diagnosis and the development of more robust predictive maintenance strategies.

To present the results, commonly used industrial feature Root Mean Square (RMS) in fault diagnosis is utilized. The feature is calculated for all operating conditions and across the four fault types, including H, IRF, ORF, and REF. The results are illustrated in Figure 6, where for each fixed radial load, the rotational speed varies from 500 rpm to 3000 rpm. As observed in the graphs, the vibration amplitude under the ORF condition is the highest compared to the other fault conditions, while the vibration amplitudes corresponding to the IRF and REF conditions are the second highest, following the ORF.

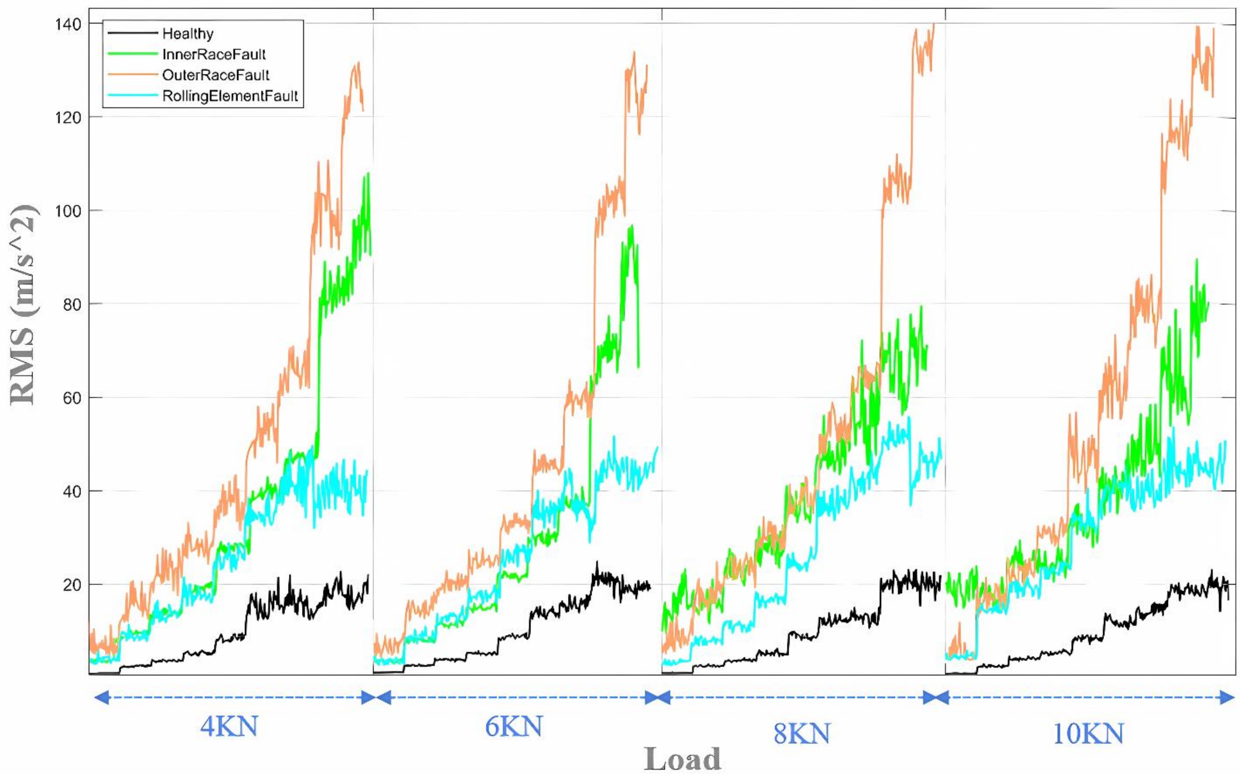

Figure 6. RMS feature representation of the four REB conditions (healthy, IRF, REF, and ORF) as rotational speed varies from 500 to 3000 rpm under fixed radial load conditions.

3.3. Industrial Data Acquisition

To evaluate the performance of the proposed model under actual industrial operating conditions, industrial data were collected from REBs used in various sectors, including mining, refining, wood, and paper industries. The dataset encompasses a wide range of REB types, such as ball, cylindrical, and barrel REBs, single-row and double-row, fixed and self-aligning, one-piece and two-piece, lubricated with grease or oil. These data also cover diverse operating conditions, including variations in speed, load, and mounting orientation (horizontal or vertical). Figure 7 illustrates examples of faults in these industrial REBs, which were visually observed after replacement and sectioning. A total of 88 datasets were recorded across four conditions, including healthy, ORF, IRF, and REF, with 22 signals per condition. This dataset provides a valuable resource for assessing the model's robustness under variable real-world operating scenarios.

a) 

b)  c) 

Figure 7. Visual inspection results of selected industrial REBs, showing examples of (a) Inner Race Fault (IRF), (b) Outer Race Fault (ORF), and (c) Rolling Element Fault (REF).

3.4. Laboratory Data Acquisition under Fixed Operating Conditions

For the re-evaluation of the proposed model's performance, an independent laboratory dataset previously collected through a series of accelerated life tests was utilized. These experiments were conducted at the Vibration Laboratory of Sharif University of Technology as part of an earlier study on the degradation behavior of REBs. In this test program, eight accelerated life tests were performed under severe loading conditions, during which vibration signals were continuously recorded using a sensor mounted on the REBs from the moment of installation until final failure. The laboratory setup corresponding to these experiments is illustrated in Figure 8. Owing to its distributional characteristics, which differ substantially from those of the initial laboratory dataset, this dataset was incorporated in the present study to rigorously assess the robustness and generalization capability of the developed model.

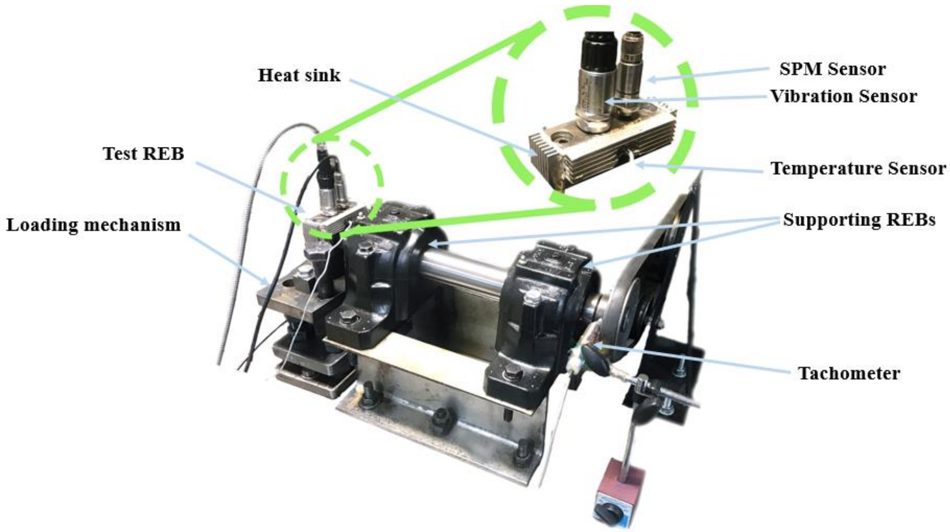

Figure 8. Accelerated life tests performed on the REB experimental test rig

In this experimental setup (Figure 8), a vibration sensor and a temperature sensor were installed on the tested REB, which was a deep groove bearing (code 6907). Accelerated life tests were performed under constant operating conditions at 2000 rpm with a radial load of 9000 N, and vibration data were recorded at a sampling frequency of 25.6 kHz. Figure 9 illustrates the damage observed in the REB components after disassembly at the end of each test. In total, 75 samples were used in this study, including 25 healthy REBs and 50 defective samples, comprising 15 with IRF, 10 with ORF, and 25 with REF.

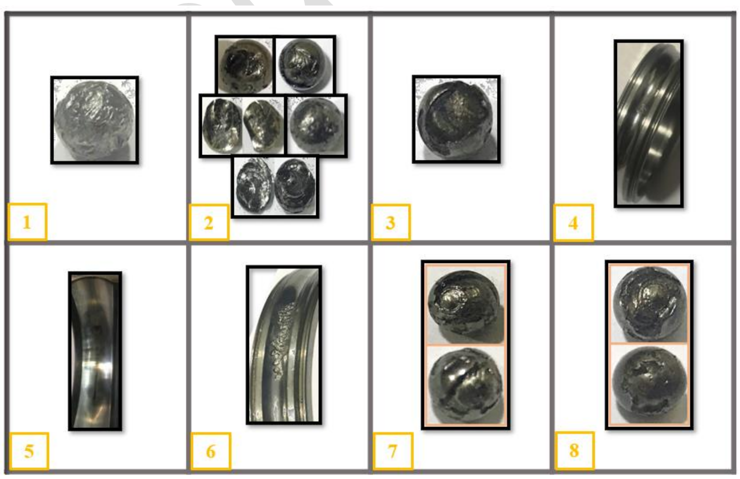

Figure 9. Visual inspection of faults in the components of REBs subjected to accelerated life testing.

Figure 10 shows the RMS trends for eight laboratory tests, from the start to the end of life.

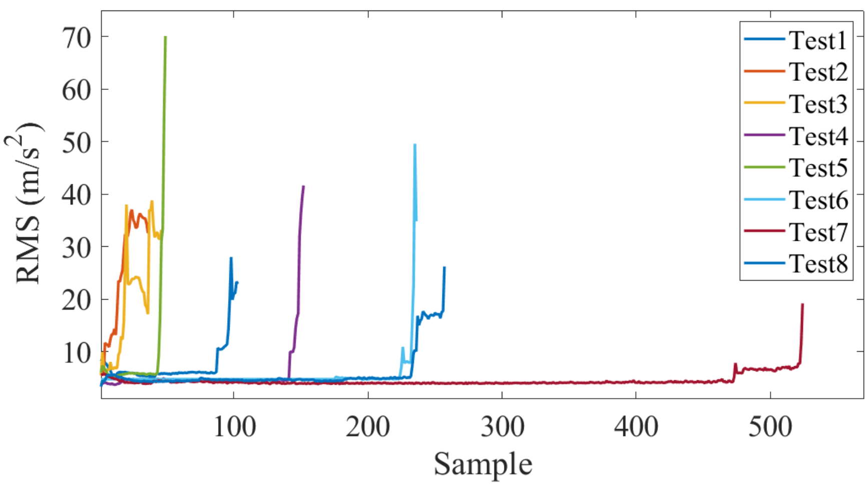

Figure 10. RMS trends observed during eight accelerated life tests.

4. Results and Discussion

To verify the effectiveness of the proposed fault detection framework, experiments were conducted using three types of datasets, including laboratory data under variable operational conditions, laboratory data under fixed operational conditions, and industrial data. The primary laboratory dataset consisted of 4,741 vibration signal samples collected under 36 different operational scenarios, with variations in rotational speed and load. These data were fully utilized to train the model and extract robust hierarchical features using SAE and DNN. To evaluate the model's performance on new data and under different conditions, the fine-tuning of the pretrained DNN output layer was performed. In this process, for each dataset separately, 5 samples from each condition (H, IRF, ORF, and REF) were selected for fine-tuning, while the remaining samples in each dataset were reserved for testing. This procedure allowed the model to be independently fine-tuned on the laboratory dataset under fixed operational conditions as well as on the industrial data, and its performance was subsequently evaluated on the unseen samples.

To address differences in sampling frequencies between datasets and align the signals, a resampling technique was applied as needed. In this process, the signal was first transformed into the frequency domain, the number of samples was adjusted using appropriate methods, and then the signal was transformed back to the time domain to preserve its overall structure. Anti-aliasing filters were also applied to minimize distortions and ensure signal integrity. This resampling procedure could be applied to either industrial data or laboratory data under fixed operational conditions whenever necessary. During fine-tuning and testing, AdaBN was applied to ensure effective alignment between different domains. The feature extraction layers remained frozen, allowing the pretrained SAE-DNN to leverage the robust features learned from the laboratory data, while the classifier adapted to new conditions. This approach enabled the accurate and reliable identification of different fault conditions under diverse operational scenarios.

The confusion matrix of the model evaluated on the industrial test data is presented in Figure 11, showing an overall classification accuracy of 92.65%. All healthy samples were correctly classified. Most misclassifications occurred between ORF and IRF or REF, consistent with the similarity of vibration signal patterns among these fault types.

For the laboratory dataset under fixed operational conditions, the resulting confusion matrix is shown in Figure 12, and the overall classification accuracy was 90.91%. All healthy samples were correctly classified, while most misclassifications occurred between ORF and IRF or REF. These results indicate that the proposed model can reliably adapt to laboratory data under both variable and fixed operational conditions, as well as industrial data, while maintaining high fault detection performance across different fault types.

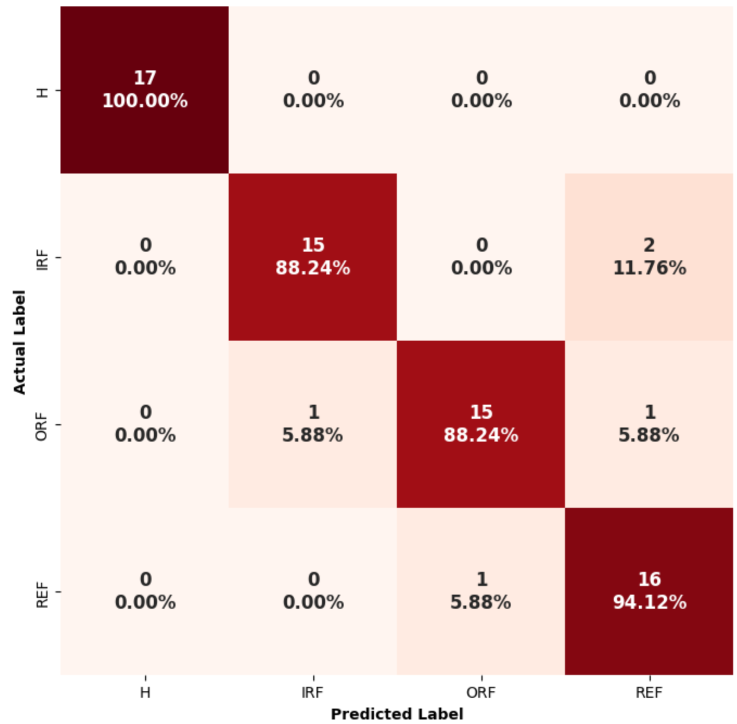

Figure 11. Confusion matrix of the proposed model evaluated on industrial test data.

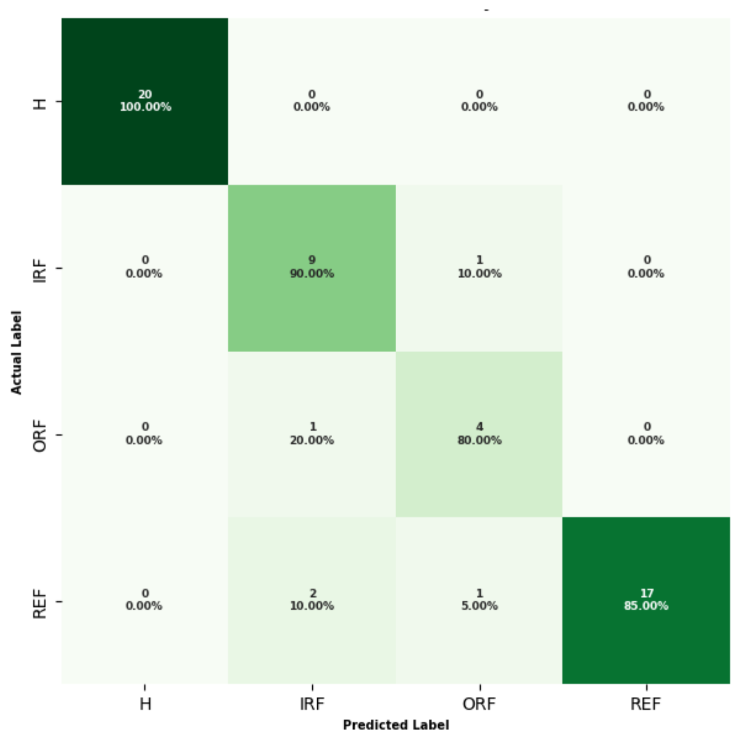

Figure 12. Confusion matrix of the proposed model evaluated on the laboratory test data under fixed operational conditions**.**

The training and validation errors were monitored throughout the learning process as a measure to evaluate the stability of the proposed model and to determine the early stopping point. It was observed that while the training error decreased steadily, the validation error plateaued or slightly increased after a certain stage, indicating a potential risk of overfitting. To mitigate overfitting and enhance the generalization capability of the proposed model on both industrial data and laboratory data under fixed operational conditions, an Early Stopping strategy was employed. The patience parameter was set to three epochs, meaning that if no significant improvement in the validation error was observed over three consecutive epochs, the training process was terminated. Using this approach, the network stopped training after 20 epochs.
Figure 13, which shows the training and validation error curves, corresponds to the industrial dataset. This strategy enables the model to effectively learn robust and discriminative features from the training data, prevent excessive fitting, and ensure high performance on unseen samples in both types of data, thereby maintaining the reliability and generalization capability of the proposed fault diagnosis framework.

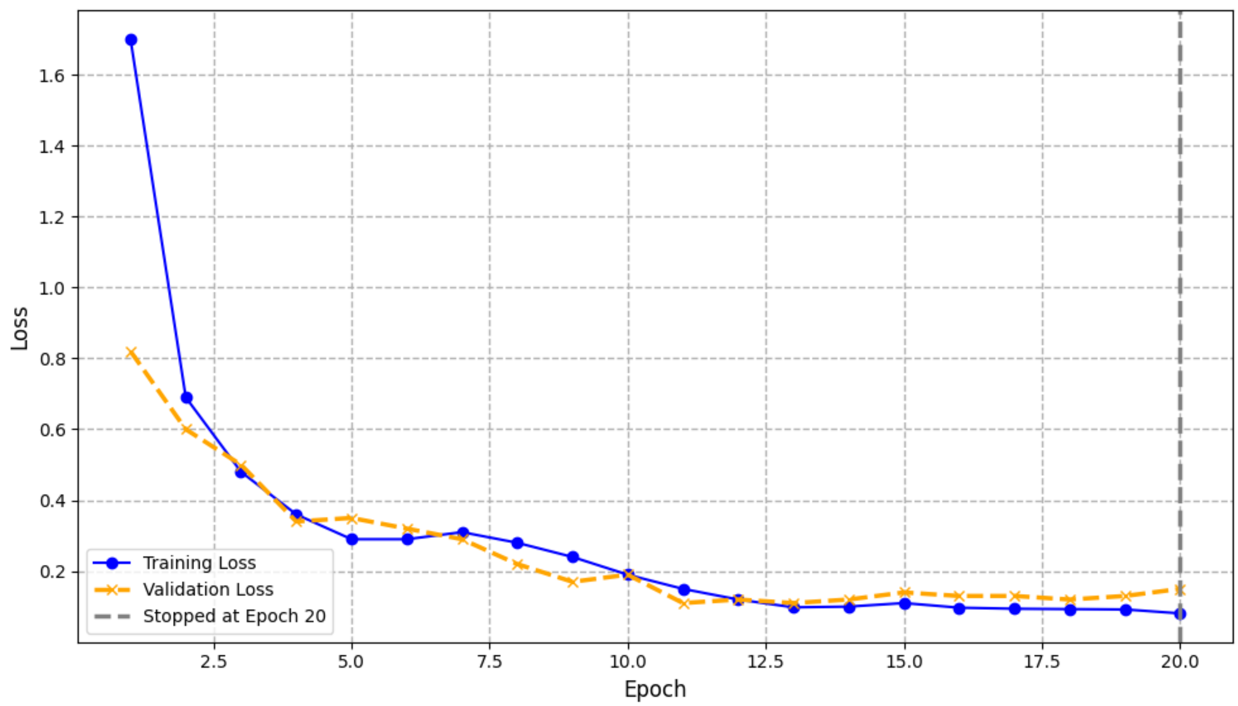

Figure 13. Training and validation error curves of the proposed model on industrial test data, illustrating the use of Early Stopping to prevent overfitting.

Following the analysis of the confusion matrices, Table 4 presents a quantitative evaluation of the proposed model on both the industrial dataset and the laboratory dataset under fixed operating conditions. Metrics include Accuracy, Precision, Recall, and F1-Score. For industrial data, healthy samples were classified perfectly, and fault classes also achieved high values, demonstrating the model's ability to generalize from laboratory training to real operating conditions. For the laboratory dataset, healthy samples were perfectly identified, and fault classes showed slightly lower metrics due to more similar vibration responses at constant speed, but overall the model still demonstrated robust fault detection. These results confirm that SAE-based hierarchical feature extraction combined with DNN classification and AdaBN alignment enables effective cross-domain generalization and reliable REB fault diagnosis.

Table 4. Performance Metrics of the Proposed Model on Industrial and Fixed-Condition Laboratory Test Data

Dataset	Fault Type	Accuracy	Precision	Recall	F1-Score
Industrial	H	1.000	1.000	1.000	1.000
	IRF	0.882	0.882	0.882	0.882
	ORF	0.882	0.900	0.882	0.891
	REF	0.941	0.882	0.941	0.911
	Overall	0.926	0.916	0.926	0.916
Laboratory Data under Fixed Operating Conditions	H	1.000	1.000	1.000	1.000
	IRF	0.900	0.818	0.900	0.857
	ORF	0.800	0.727	0.800	0.762
	REF	0.850	0.857	0.850	0.854
	Overall	0.909	0.851	0.888	0.857

Table 5 summarizes the proposed model's performance for each fault class on both industrial and fixed-condition laboratory datasets, reporting Sensitivity, Specificity, and False Negative Rate. For industrial data, all healthy samples were correctly classified, and fault classes achieved high Sensitivity (IRF and ORF 0.882, REF 0.941), with occasional misclassifications among similar faults. For the laboratory dataset, healthy samples were perfectly identified, and Sensitivity for faults ranged from 0.80 to 0.90, while Specificity remained high. Overall, the model demonstrates robust REB fault detection across both real and controlled environments, with low false negative rates.

Table 5. Evaluation Metrics of the Proposed Model for Each Fault Condition on Industrial and Fixed-Condition Laboratory Test Data

Dataset	Fault Type	Sensitivity (TP / (TP+FN))	Specificity (TN / (TN+FP))	False Negative Rate (FN / (TP+FN))
Industrial	H	1.000	1.000	0.000
	IRF	0.882	0.980	0.118
	ORF	0.882	0.985	0.118
	REF	0.941	0.954	0.059
Laboratory Data under Fixed Operating Conditions	H	1.000	1.000	0.000
	IRF	0.900	0.963	0.100
	ORF	0.800	0.953	0.200
	REF	0.850	0.969	0.150

To compare and evaluate the contribution of each component in the proposed framework, a base version of the model was also assessed. This version includes only the SAE, DNN, and AdaBN components, without performing fine-tuning of the output layer. Such a configuration is similar to certain methods reported in previous studies and allows for assessing the impact of the fine-tuning stage on overall model performance. When applied to the industrial dataset, this base model achieved an overall accuracy of 80.88%, while for the laboratory dataset under fixed operational conditions, the accuracy decreased to 76.36%. The corresponding confusion matrices for these two datasets are presented in Figures 14a and 14b, indicating that most misclassifications occurred between the ORF and IRF or REF classes, which is consistent with the similarity of vibration signal patterns for these fault types.

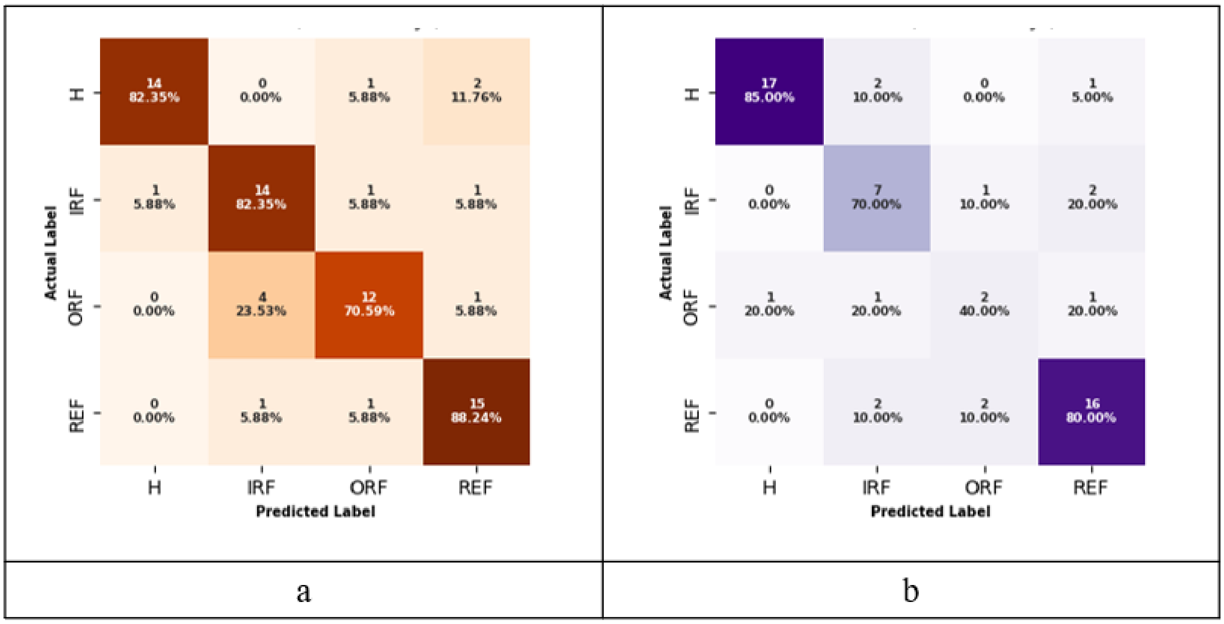

Figure 14. Confusion matrices of the base model without fine-tuning: (a) industrial dataset, (b) laboratory dataset under fixed operating conditions.

Table 6 summarizes the overall accuracy of both the base model and the full proposed framework across the two datasets. The results demonstrate that the base model performs adequately only when the distribution of the test data closely matches that of the training data. In cases where the test data distribution differs significantly from the training set, such as when industrial data or laboratory data under fixed operating conditions are used, the performance of the base model drops sharply. This decrease in accuracy occurs because, without the selective fine-tuning of the output layer, the base model cannot effectively adjust to variations in feature distributions or account for domain-specific patterns present in the target data. In contrast, the full proposed framework, which incorporates both AdaBN for domain alignment and limited fine-tuning of the classifier output layer, maintains high accuracy and robust fault classification across both laboratory and industrial datasets. These findings clearly highlight the essential role of the fine-tuning stage in ensuring stable and reliable performance when the model encounters target domains with distributions that differ from the source training data.

Table 6. Comparison of Classification Accuracy for the Proposed and Base Models on Industrial and Fixed-Condition Laboratory Datasets

Dataset	Proposed Model (with Fine-Tuning)	Base Model (No Fine-Tuning)
Industrial	92.65%	80.88%
Laboratory Data under Fixed Operating Conditions	90.91%	76.36%

5. Summary/ Conclusions

In this study, a comprehensive fault detection framework for REBs was proposed. The framework integrates hierarchical feature extraction via a SAE, classification with a DNN, and domain adaptation using AdaBN. The model was initially trained on extensive laboratory data under variable operating conditions and subsequently evaluated on both a secondary laboratory dataset under fixed operating conditions and an industrial dataset. For both industrial and fixed-condition laboratory datasets, a small subset of labeled samples from each fault condition was used to fine-tune only the output layer, while the remaining samples were reserved for testing. For comparison, a baseline version of the model was also assessed, in which the fine-tuning stage was omitted, leaving only SAE, DNN, and AdaBN. Results showed that this baseline model performs well only when the test data distribution closely matches that of the training data. When the test data distribution differs from the training set, performance drops significantly, emphasizing the importance of the fine-tuning stage for robust generalization. Experimental results demonstrate that the full proposed framework with fine-tuning achieves high accuracy, Precision, Recall, and F1-Score across various fault types, reaching overall accuracies of 92.65% for industrial data and 90.91% for fixed-condition laboratory data. Low false negative rates and high specificity for healthy REBs further confirm the reliability of the approach in practical applications. These findings highlight that combining SAE for robust feature extraction, AdaBN for domain adaptation, and selective fine-tuning of the output layer is essential for stable generalization from laboratory to industrial environments. Overall, the proposed framework provides a robust, reliable, and practical solution for predictive maintenance and fault diagnosis of REBs under diverse operational conditions.

Acknowledgments

The authors would like to express their sincere gratitude to *Behravesh Vibration Engineering Company* for their valuable support in data collection and for providing essential technical assistance throughout the research.

References

[1] Mobley, R.K. An Introduction to Predictive Maintenance; Elsevier: Amsterdam, The Netherlands, 2002.

[2] Cui, W.; Meng, G.; Gou, T.; Wang, A.; Xiao, R.; Zhang, X. Intelligent rolling bearing fault diagnosis method using symmetrized dot pattern images and CBAM-DRN. Sensors 2022, 22, 9954.

[3] Bhagwan, S. A review of various techniques used for shaft failure analysis. Asian J. Multidimens. Res. 2021, 10, 387–392.

[4] Guo, H.; Ping, D.; Wang, L.; Zhang, W.; Wu, J.; Ma, X.; Xu, Q.; Lu, Z. Fault Diagnosis Method of Rolling Bearing Based on 1D Multi-Channel Improved Convolutional Neural Network in Noisy Environment. Sensors. 2025, 25, 2286.

[5] Song, X.; Cong, Y.; Song, Y.; Chen, Y.; Liang, P. A bearing fault diagnosis model based on CNN with wide convolution kernels. J. Ambient. Intell. Humaniz. Comput. 2022, 13, 4041–4056.

[6] Chen, X.; Zhang, B.; Gao, D. Bearing fault diagnosis based on multi-scale CNN and LSTM model. J. Intell. Manuf. 2021, 32, 971–987.

[7] Jia, F.; Lei, Y.; Lin, J.; Zhou, X.; Lu, N. Deep neural networks: A promising tool for fault characteristic mining and intelligent diagnosis of rotating machinery with massive data. Mech. Syst. Signal Process. 2016, 72, 303–315.

[8] Xu, G.; Liu, M.; Jiang, Z.; Söffker, D.; Shen, W. Bearing fault diagnosis method based on deep convolutional neural network and random forest ensemble learning. Sensors 2019, 19, 1088.

[9] Eren, L. Bearing fault detection by one-dimensional convolutional neural networks. Math. Probl. Eng. 2017, 2017, 8617315.

[10] Chen, J.; Jiang, J.; Guo, X.; Tan, L. An efficient CNN with tunable input-size for bearing fault diagnosis. Int. J. Comput. Intell. Syst. 2021, 14, 625–634.

[11] Peng, D.; Wang, H.; Liu, Z.; Zhang, W.; Zuo, M.J.; Chen, J. Multibranch and multiscale CNN for fault diagnosis of wheelset bearings under strong noise and variable load condition. IEEE Trans. Ind. Inf. 2020, 16, 4949–4960.

[12] Zhu, X.; Luo, X.; Zhao, J.; Hou, D.; Han, Z.; Wang, Y. Research on deep feature learning and condition recognition method for bearing vibration. Appl. Acoust. 2020, 168, 107435.

[13] Peng, D.; Wang, H.; Desmet, W.; Gryllias, K. RMA-CNN: A residual mixed-domain attention CNN for bearings fault diagnosis and its time-frequency domain interpretability. J. Dyn. Monit. Diagn. 2023, 2, 115–132.

[14] Wang, B.; Feng, G.; Huo, D.; Kang, Y. A bearing fault diagnosis method based on spectrum map information fusion and convolutional neural network. Processes 2022, 10, 1426.

[15] Pham, M.T.; Kim, J.M.; Kim, C.H. Accurate bearing fault diagnosis under variable shaft speed using convolutional neural networks and vibration spectrogram. Appl. Sci. 2020, 10, 6385.

[16] Zhang, W.; Peng, G.; Li, C. Rolling element bearings fault intelligent diagnosis based on convolutional neural networks using raw sensing signal. In Advances in Intelligent Information Hiding and Multimedia Signal Processing: Proceedings of the Twelfth International Conference on Intelligent Information Hiding and Multimedia Signal Processing, Kaohsiung, Taiwan, 21–23 November 2016; Springer International Publishing: Berlin/Heidelberg, Germany, 2016 ; Volume 2, pp. 77–84.

[17] Hasan, M.J.; Islam, M.M.; Kim, J.M. Bearing fault diagnosis using multidomain fusion-based vibration imaging and multitask learning. Sensors 2021, 22, 56.

[18] Qin, Y.; Shi, X. Fault diagnosis method for rolling bearings based on two-channel CNN under unbalanced datasets. Appl. Sci. 2022, 12, 8474.

[19] Xin, Y.; Li, S.; Wang, J.; An, Z.; Zhang, W. Intelligent fault diagnosis method for rotating machinery based on vibration signal analysis and hybrid multi-object deep CNN. IET Sci. Meas. Technol. 2020, 14, 407–415.

[20] Kannan, V.; Zhang, T.; Li, H. A review of the intelligent condition monitoring of rolling element bearings. Machines 2024, 12, 484.

[21] Wang, Z.; Xu, X.; Song, D.; Zheng, Z.; Li, W. A Novel Bearing Fault Diagnosis Method Based on Improved Convolutional Neural Network and Multi-Sensor Fusion. Machines 2025, 13, 216.

[22] Kiakojouri, A.; Wang, L. A Generalized Convolutional Neural Network Model Trained on Simulated Data for Fault Diagnosis in a Wide Range of Bearing Designs. Sensors 2025, 25, 2378.

[23] Tayyab, S.M.; Chatterton, S.; Pennacchi, P. Intelligent defect diagnosis of rolling element bearings under variable operating conditions using convolutional neural network and order maps. Sensors 2022, 22, 2026.

[24] Shen, F.; Chen, C.; Yan, R.; Gao, R.X. Bearing fault diagnosis based on SVD feature extraction and transfer learning classification. In Proceedings of the 2015 Prognostics and System Health Management Conference (PHM), Beijing, China, 21–23 October 2015; IEEE: Piscataway, NJ, USA, 2015; pp. 1–6.

[25] Zhang, W.; Peng, G.; Li, C.; Chen, Y.; Zhang, Z. A new deep learning model for fault diagnosis with good anti-noise and domain adaptation ability on raw vibration signals. Sensors 2017, 17, 425.

[26] Zhang, B.; Li, W.; Tong, Z.; Zhang, M. Bearing fault diagnosis under varying working condition based on domain adaptation. arXiv 2017, arXiv:1707.09890.

[27] Zhang, R.; Tao, H.; Wu, L.; Guan, Y. Transfer learning with neural networks for bearing fault diagnosis in changing working conditions. IEEE Access 2017, 5, 14347–14357.

[28] Qian, W.; Li, S.; Wang, J.; Xin, Y.; Ma, H. A new deep transfer learning network for fault diagnosis of rotating machine under variable working conditions. In Proceedings of the 2018 Prognostics and System Health Management Conference (PHM-Chongqing), Chongqing, China, 26–28 October 2018; IEEE: Piscataway, NJ, USA, 2018; pp. 1010–1016.

[29] Tong, Z.; Li, W.; Zhang, B.; Zhang, M. Bearing fault diagnosis based on domain adaptation using transferable features under different working conditions. Shock Vib. 2018, 2018, 6714520.

[30] Tong, Z.; Li, W.; Zhang, B.; Jiang, F.; Zhou, G. Bearing fault diagnosis under variable working conditions based on domain adaptation using feature transfer learning. IEEE Access 2018, 6, 76187–76197.

[31] Yang, B.; Lei, Y.; Jia, F.; Xing, S. An intelligent fault diagnosis approach based on transfer learning from laboratory bearings to locomotive bearings. Mech. Syst. Signal Process. 2019, 122, 692–706.

[32] Li, X.; Jiang, H.; Zhao, K.; Wang, R. A deep transfer nonnegativity-constraint sparse autoencoder for rolling bearing fault diagnosis with few labeled data. IEEE Access 2019, 7, 91216–91224.

[33] Shao, S.; McAleer, S.; Yan, R.; Baldi, P. Highly accurate machine fault diagnosis using deep transfer learning. IEEE Trans. Ind. Informatics. 2018, 15, 2446–2455.

[34] Zhiyi, H.; Haidong, S.; Lin, J.; Junsheng, C.; Yu, Y. Transfer fault diagnosis of bearing installed in different machines using enhanced deep auto-encoder. Measurement 2020, 152, 107393.

[35] Zhao, B.; Zhang, X.; Zhan, Z.; Pang, S. Deep multi-scale convolutional transfer learning network: A novel method for intelligent fault diagnosis of rolling bearings under variable working conditions and domains. Neurocomputing 2020, 407, 24–38.

[36] Li, X.; Jia, X.D.; Zhang, W.; Ma, H.; Luo, Z.; Li, X. Intelligent cross-machine fault diagnosis approach with deep auto-encoder and domain adaptation. Neurocomputing 2020, 383, 235–247.

[37] Wu, Z.; Jiang, H.; Lu, T.; Zhao, K. A deep transfer maximum classifier discrepancy method for rolling bearing fault diagnosis under few labeled data. Knowl.-Based Syst. 2020, 196, 105814.

[38] Dong, Y.; Li, Y.; Zheng, H.; Wang, R.; Xu, M. A new dynamic model and transfer learning based intelligent fault diagnosis framework for rolling element bearings race faults: Solving the small sample problem. ISA Trans. 2022, 121, 327–348.

[39] Chen, X.; Yang, R.; Xue, Y.; Huang, M.; Ferrero, R.; Wang, Z. Deep transfer learning for bearing fault diagnosis: A systematic review since 2016. IEEE Trans. Instrum. Meas. 2023, 72, 3508221.

[40] Zhong, Z.; Xie, H.; Wang, Z.; Zhang, Z. Domain Adversarial Transfer Learning Bearing Fault Diagnosis Model Incorporating Structural Adjustment Modules. Sensors 2025, 25, 1851.

[41] Feisa, T. T., Gebremedhen, H. S., Kibrete, F., Woldemichael, D. E., Ageze, S. D., & Nega, H. D. (2025). *A Comprehensive Review of Deep Transfer Learning for Intelligent Fault Diagnosis in Rotating Machines*. Journal of Mechanical Engineering Research.

[42] Song, L., Zhao, Y., He, J., Wang, S., Zhong, B., & Wang, F. (2023). MAJATNet: A Lightweight Multi-Scale Attention Joint Adaptive Adversarial Transfer Network for Bearing Unsupervised Cross-Domain Fault Diagnosis. *Sensors*, 23(4), 1234.

[43] Che, J., Fang, L., Ma, Q., Yu, G., Sun, X., & Zhu, X. (2023). An Intelligent Bearing Fault Transfer Diagnosis Method Based on Improved Domain Adaptation. *IEEE Transactions on Industrial Informatics*.

[44] Deveci, B. U., Celtikoglu, M., Albayrak, O., Unal, P., & Kirci, P. (2023). Transfer Learning Enabled Bearing Fault Detection Methods Based on Image Representations of Single-Dimensional Signals. *Measurement*, 206, 112567.

[45] Xing, Z., Liu, Y., Wang, Q., & Fu, J. (2023). Fault Diagnosis of Rotating Parts Integrating Transfer Learning and ConvNeXt Model. *IEEE Access*, 11, 34567–34579.

[46] Guo, Y., Cheng, Z., Zhang, J., Sun, B., & Wang, Y. (2023). A Review on Adversarial-Based Deep Transfer Learning Mechanical Fault Diagnosis. *Mechanical Systems and Signal Processing*.

[47] Tang, Z., Hou, X., Huang, X., Wang, X., & Zou, J. (2023). Domain Adaptation for Bearing Fault Diagnosis Based on SimAM and Adaptive Weighting Strategy. *IEEE Transactions on Industrial Electronics*.

[48] Liu, C., Hu, R., Fang, X., Luo, W., & Zhu, C. (2023). Enhancing Unsupervised Bearing Fault Diagnosis Through Structured Prediction in Latent Subspace. *Mechanical Systems and Signal Processing*, 186, 109946.

[49] Li, X., Yu, T., Li, D., Wang, X., Shi, C., Xie, Z., & Kong, X. (2023). A Migration Learning Method Based on Adaptive Batch Normalization Improved Rotating Machinery Fault Diagnosis. *Journal of Manufacturing Systems*, 66, 101–115.

[50] Zhong, Z., Xie, H., Wang, Z., & Zhang, Z. (2023). Domain Adversarial Transfer Learning Bearing Fault Diagnosis Model Incorporating Structural Adjustment Modules. *Applied Sciences*, 13(12), 6745.

[51] Bearing Data Center. Available online: https://engineering.case.edu/bearingdatacenter (accessed on).

[52] SDT, Vigilant. Available online: https://sdtultrasound.com/products/permanent-monitoring/vigilant/ (accessed on).

[53] SKF Bearing Select. Available online: https://skfbearingselect.com/#/size-lubrication/single-bearing (accessed on).